VIP *Very Important Paper*

Probing the Origin of Overpotential for Sodium-Oxygen Batteries with Distribution of Relaxation Time

Dejing Ma[+],[a] Juan Chen[+],[a] Fengjiao Yu,*[a] and Yuhui Chen*[a]

Sodium-oxygen batteries are emerging as new battery systems. Deep understanding of the origin of overpotential and the kinetic process in sodium-oxygen batteries remain challenging yet critical. We apply a method of distribution of relaxation time (DRT) to decipher the electrochemical impedance spectroscopy (EIS), allowing us to monitor the changes of different kinetic processes during the discharging and charging. The origin of the overpotential in a battery was further comprehensively investigated combining DRT analysis with differential electrochemical mass spectrometry, Raman and other characterizations. Overpotential is found to primarily stem from oxygen mass transport during discharging, and from poor solid-solid contact at the electrode surface during charging. Our work demonstrates the study of kinetic processes using DRT analysis, and suggests effective ways to improve the performances of sodium-oxygen batteries.

Introduction

Recently, pollution has reached alarming levels. Fortunately, there are various strategies to address this issue, with battery technology emerging as one of the most promising solutions. Over the past few decades, a multitude of battery types have been developed, including lithium-ion, sodium-ion, and metal-oxygen batteries.[1] Among these, the sodium-oxygen battery stands out, particularly since Janek and his team introduced a groundbreaking reversible sodium-oxygen battery based on NaO_2 formation and decomposition.[2] This innovation has garnered significant attention due to its impressive energy density, estimated at approximately 1105 Wh/kg based on NaO_2, which is three time higher than that of lithium-ion batteries.[3]

However, despite its potential, the sodium-oxygen battery faces challenges. The main discharging product, sodium superoxide (NaO_2), is insulating, complicating the subsequent charging process.[4] Consequently, both the discharging and charging voltage plateaus deviate from their thermodynamic equilibrium voltage (2.27 V vs. Na^+/Na).[5] Furthermore, polarization significantly hampers the performance and widespread adoption of Na-O₂ batteries. Therefore, it is imperative to investigate the origin of these overpotentials to overcome these hurdles and advance this promising technology.

In recent years, considerable research attention has been directed towards understanding this issue. For instance, Vegge et al. employed free energy calculations to explore overpotential phenomena.[6] However, despite these efforts, robust methodologies remain elusive. Electrochemical impedance spectroscopy (EIS) emerges as a promising tool due to its non-invasive nature and ability to track changes during discharging and charging cycles effectively. Nonetheless, interpreting EIS data poses challenges, as it encompasses a blend of electrochemical processes such as SEI passivation, charging transfer, and mass transport. This amalgamation makes it difficult to isolate individual processes, hindering direct identification of overpotential origins solely through EIS.

Although equivalent circuits are commonly employed to interpret EIS outcomes, the inherent non-uniqueness of these circuits introduces a level of unreliability. Distribution of relaxation time (DRT) offers a solution by utilizing characteristic time constants to disentangle the various electrochemical processes. DRT has demonstrated success in elucidating mechanisms in several electrochemical systems, including lithium-ion and lithium-oxygen batteries.[7] Consequently, it presents a reliable approach for decoupling electrochemical processes from EIS data and investigating the kinetic processes.

In our study, we intermittently rested the Na-O₂ battery for 1 h to conduct *in situ* EIS tests while simultaneously collecting relevant voltage data. Moreover, we analyzed gas evolution during the charging process using differential electrochemical mass spectrometry (DEMS), and subsequently characterized pertinent products post-discharge and recharge via scanning electron microscopy (SEM) and Raman spectroscopy. In addition, we employed DRT analysis to decipher the EIS results, allowing us to monitor the discharging and charging processes in Na-O₂ batteries and pinpoint the primary source of overpotential.

Results and Discussion

As illustrated in Figure 1a, the discharging plateau is at approximately 2.0 V, while the charging plateau is around 2.4 V, both observed at a current density of 0.2 mA cm⁻². This

[a] D. Ma,[+] J. Chen,[+] F. Yu, Y. Chen
State Key Laboratory of Materials-Oriented Chemical Engineering,
College of Chemical Engineering,
Nanjing Tech University,
Nanjing, Jiangsu, 211816, China
E-mail: cheny@njtech.edu.cn
fjyu@njtech.edu.cn

[+] The authors contribute equally to this work.

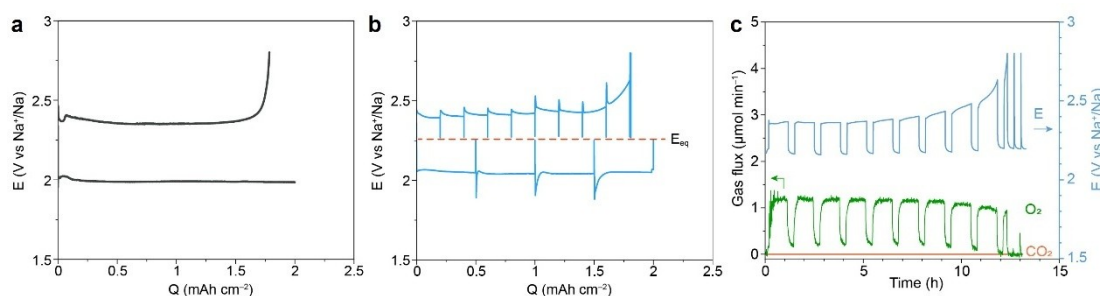📖 Supporting information for this article is available on the WWW under
https://doi.org/10.1002/batt.202400257

Batteries & Supercaps

Research Article
doi.org/10.1002/batt.202400257

Chemistry Europe
European Chemical
Societies Publishing

Figure 1. (a) Load curve of the battery with Super P composite electrode in 0.5 M NaOTf DEGDME at 0.2 mA cm^{-2}. (b) Load curve of the battery with Super P composite electrode in 0.5 M NaOTf DEGDME with resting for 1 h between each discharging/charging at 0.2 mA cm^{-2}. (c) O_2 and CO_2 gas evolution during charging examined by *in situ* DEMS with Ar as the carrier gas.

discrepancy of 400 mV between the charging and discharging plateaus is notable.

The battery was not fully discharged because the charge process would be difficult to undergo if we discharge the battery to lower potential. The discharge product NaO_2 is difficult to decompose completely due to the loss of contact (Figure S1). For electrochemical impedance spectroscopy (EIS) measurements, the cell was allowed to rest for 1 hour to achieve equilibrium, occurring every 0.5 mAh during discharging and 0.2 mAh during charging. During these rest periods, the cell's potential rapidly returned to the equilibrium potential of ca. 2.27 V, as depicted in Figure 1b. The consistency of potentials suggests symmetry in the charging and discharging processes, indicating reversible formation and decomposition of NaO_2.

Additionally, both discharging and charging curves exhibit an initial overpotential, likely attributable to the nucleation overpotential.[8] During the charging process, this overpotential may come from electrolyte decomposition during the initial stages, similar to observations in lithium-oxygen batteries.[9] Further exploration of this phenomenon will be discussed below.

Differential electrochemical mass spectrometry (DEMS) was utilized to detect the evolution of O_2 and CO_2 during charging. The evolution of oxygen was evident (Figure 1c), while no CO_2 release was detected, indicating the decomposition of NaO_2 during charging. Until the latter stages of the charging process, the amount of O_2 began to decrease as the potential rose.

In situ electrochemical impedance spectroscopy (EIS) and distribution of relaxation time (DRT) analysis were employed to dissect individual electrochemical processes and track their variations throughout the complete charging and discharging cycles. EIS measurements were conducted using a three-electrode cell, with detailed experimental procedures provided in the Supplementary Information. During EIS analysis, an alternating current signal was applied to stimulate the electrochemical system, and the corresponding voltage response was recorded.

Through DRT analysis, each electrochemical process was isolated and monitored across the discharging-charging cycle. Notably, After the battery was discharged to a capacity of 0.5 mAh, a potentiostatic electrochemical impedance

spectroscopy(PEIS) test was performed, several processes were observed at the positive electrode, as illustrated in Figure 2b. Therefore, the low-frequency signal below 1 Hz vanished upon replacing the oxygen atmosphere with argon (Figure 2a), indicating its association with O_2 diffusion. Furthermore, Kramers-Kronig (K–K) transformation revealed some distortion in the low-frequency region (see Figure S2). Consequently, the low-frequency signal was excluded from further analysis in subsequent discussions.

To assign peaks in the distribution of relaxation time (DRT) analysis, it is imperative to conduct control experiments to correlate each peak with its respective electrochemical process. As depicted in Figure 2b, four peaks, labeled τ_1-τ_4, emerge in the high-frequency region. Specifically, τ_1 and τ_2 correspond to inner resistance and ion transport across the interface, respectively .[10]

Peaks τ_3 and τ_4 fall within the charging transfer resistance (R_{ct}) range.[11] To identify the charging transfer process, if a peak decreases when an overpotential is applied, it can be attributed to R_{ct}. As illustrated in Figure 2b, both peaks τ_3 and τ_4 decrease with a -50 mV overpotential under O_2 conditions, indicating their association with the charging transfer process of oxygen reduction.

The results from differential electrochemical mass spectrometry (DEMS) primarily suggest the presence of NaO_2(Figure 1c), given that the discharging reaction primarily involves oxygen reduction. However, the formation of NaO_2 leaves a possibility of forming Na_2O_2, as their thermodynamic potentials are close. Despite this, only NaO_2 was detected in the discharging product, with no observed signal of Na_2O_2 in Raman spectra (Figure 3a). Nevertheless, compared with scanning electron microscopy (SEM) of the pristine electrode shown in Figure S3, SEM of the electrode after discharging reveals two types of discharging products: cubic NaO_2 and surface species, potentially NaO_2 or Na_2O_2 in a surface state (Figure 3b). By the way, the SEM image of the pristine electrode is shown in Figure S3. Yet, precise chemical composition information is lacking, prompting us to designate it as $NaO_{x(ads)}$. Consequently, peaks τ_3 and τ_4 correspond to the formation process of these two components, respectively. One contributes to the generation of $NaO_{x(ads)}$, which is adsorbed at the electrode surface, while the other peak can be assigned to the reduction of O_2 to
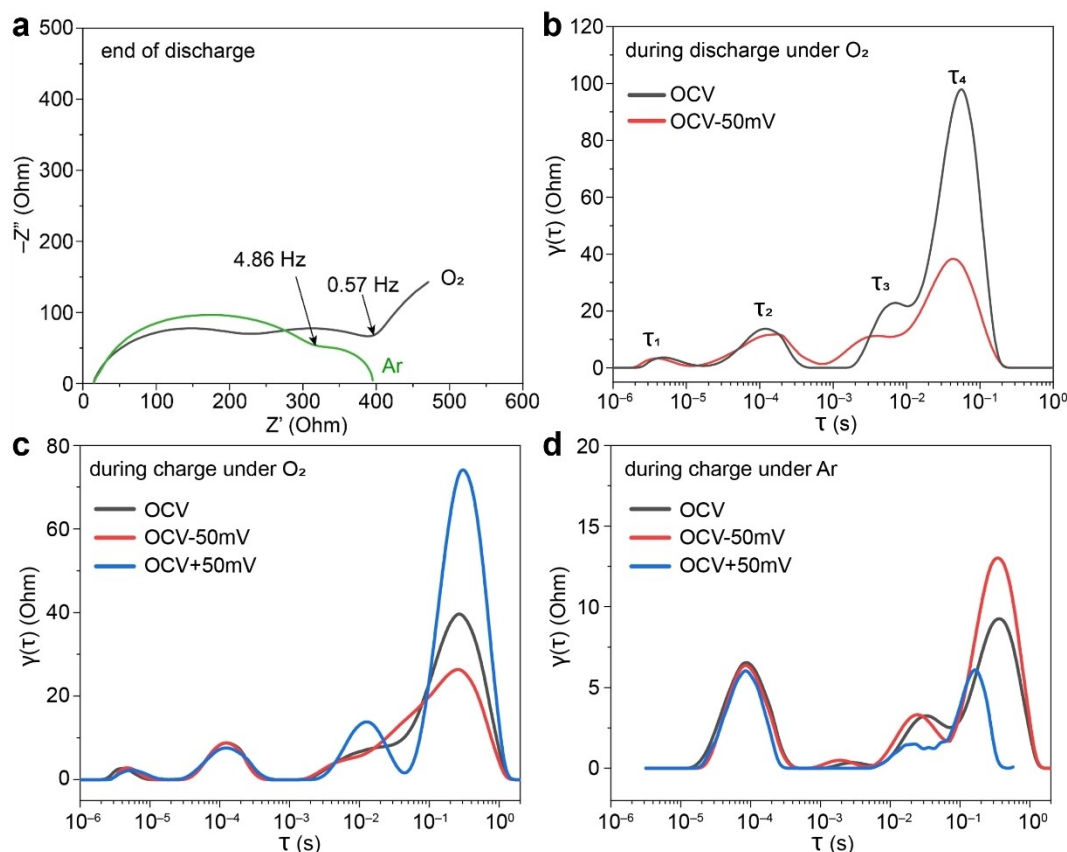
Figure 2. (a) Nyquist plots at the end of discharging under O_2 and Ar. (b) DRT analysis of EIS during discharging under O_2 at OCV with an applied overpotential of 50 mV. DRT analysis of EIS during charging at OCV with an applied overpotential of 50 mV under (c) O_2 and (d) Ar.

superoxide in the solution phase, followed by diffusion and growth into crystal structures, as depicted by NaO_2 cubes ($NaO_{2(sol)}$).

During discharging, *in situ* electrochemical impedance spectroscopy (EIS) coupled with distribution of relaxation time (DRT) analysis was performed at open circuit voltage (OCV) following a 1-hour equilibrium period (Figure 3c & d). Notably, during discharging, the τ_2 peak exhibits a slight increase, indicative of surface layer thickening at the electrode. Conversely, increase of τ_3 peak coincides with a decrease in τ_4 peak, implying that the surface layer thickens concurrently with the formation of $NaO_{x(ads)}$, thereby making charging transfer more difficult. Concurrently, the reaction involving $NaO_{x(ads)}$ assumes greater prominence due to the surface coverage by NaO_x. With surface gradually coverage by NaO_x, the surface $NaO_{x(ads)}$ become a major reaction.

Our prior work also studied into this aspect, highlighting the difference between the impedance characteristics of metal-air batteries and lithium-ion batteries.[12] In metal-air batteries, the process resembles a complex catalytic phenomenon. In lithium-ion batteries, even though multiple processes of lithium-ion intercalation may occur, the active area of electrode reaction remains relatively stable (unless significant particle degradation occurs). Therefore, the charge transfer difficulty can be directly measured through R_{ct}.

Metal-air batteries operate through catalytic conversion reactions where the active sites on electrodes or catalyst surfaces are engaged in multiple dynamic processes, often in competition. For instance, in this study, there is a competition between $NaO_{x(ads)}$ and $NaO_{2(sol)}$. As $NaO_{x(ads)}$ covers the active sites on the electrode surface, the charge transfer resistance (R_{ct}) of oxygen reduction reaction (ORR) at individual sites increases, while its contribution to the overall electrode process decreases continuously. This leads to a decrease in the overall DRT peak corresponding to ORR across all surface sites (Figure 3d). Consequently, the τ_3 peak increases while the τ_4 peak decreases during the discharge process.

We observe that the overall overpotential during discharge is relatively low, around 200 mV. Furthermore, the primary reaction involves a single electron transfer process. It is unlike multi-electron processes that include various thermodynamic overpotentials and multiple charge transfer steps. Analysis of the EIS data suggests that the adverse impact of electrode surface passivation on ionic migration and charge transfer is not significant. The main reason for electrode passivation is the common by-products of inorganic and organic carbonate. However, post-discharge titration revealed that only 0.4% Na_2CO_3 and 1.7% organic carbonate of the expected NaO_2 amount were detected in the electrode (Figure S4), significantly lower than the levels of lithium carbonate found in lithium-oxygen batteries.[13] This finding reinforces our earlier discussion
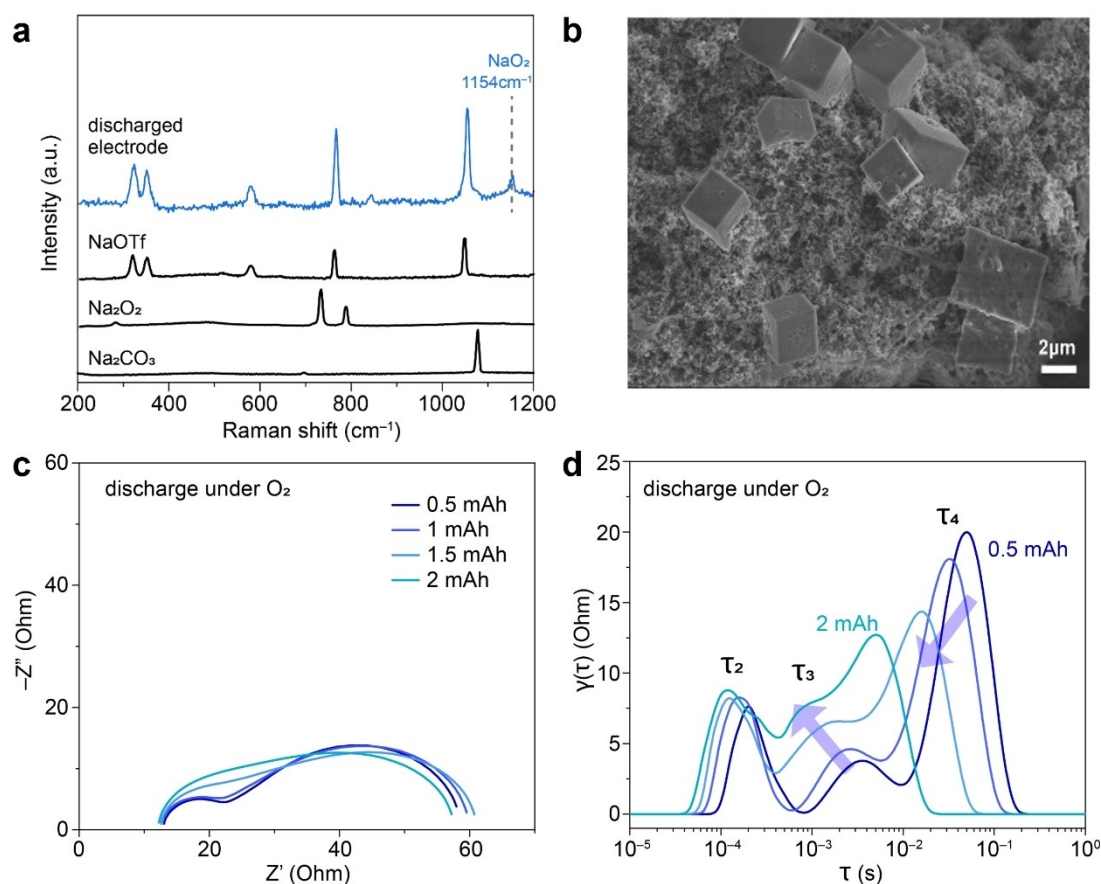
Figure 3. (a) Raman spectra of the composite electrode after discharging. (b) SEM image of the composite electrode after discharging. (c) Nyquist plots during discharging under O_2. (d) Corresponding DRT analysis of discharging under O_2.

that the negative consequences of carbonate passivation are not severe. Moreover, in conjunction with Figure 1, we propose that the primary overpotential during discharge largely arises from the low oxygen concentration in the electrolyte and the oxygen mass transport process. During the charging they cannot be decomposed until charge potential is up to its thermodynamic potential which is 3.4 V (vs. Na^+/Na). The cut-off charging potential in our work is 2.8 V (vs.Na^+/Na), which is not enough to decompose carbonate species.

During the charge process, we employed the same approach to assess the charge transfer resistance (R_{ct}) within the DRT analysis. Surprisingly, the τ_3 and τ_4 peaks at open circuit voltage (OCV) exhibited an unexpected trend, when electric potential was applied (Figure 2c). Specifically, τ_3 and τ_4 peak increased when a positive overpotential of $+50$ mV was applied, whereas it decreased with a negative overpotential of -50 mV. This suggests that while the DRT peak at OCV corresponds to the charge transfer process, it is not indicative of the charging process but the oxygen reduction process associated with discharge. Given the small overpotential during discharge, EIS measurements might capture signals from the oxygen reduction reaction (ORR) segment, complicating the evaluation of the source of charge overpotential.

To exclude the interference of O_2, further investigation was conducted under an Ar atmosphere. After the battery was

charged to a capacity of 0.2 mAh, a potentiostatic electrochemical impedance spectroscopy test was carried out. (Figure 2d). As to τ_1, the high frequency part was easy to be interfered by inductance when we operate under Ar. As a result, we cut the max frequency. But it is ok since the main purpose here is to detect the DRT peak of R_{ct} which show up in mid-frequency.It revealed that the R_{ct} related to the charging oxidation falls within a similar range. The DRT peaks correspond to the charge transfer of NaO_2 decomposition. Additionally, comparison indicates that the R_{ct} of the same battery under Ar is smaller than that under O_2, making it susceptible to being overwritten and interfered with by signals under O_2. Therefore, to mitigate the influence of ORR, we employed two methods. Firstly, we changed the charging atmosphere to Ar. Secondly, we utilized galvanostatic electrochemical impedance spectroscopy (GEIS), similar to galvanostatic charge but with a very small current, to maintain the battery charging at a constant voltage of 2.4 V, thereby suppressing interference from ORR.

Potentiostatic electrochemical impedance spectroscopy (PEIS) was initially conducted under an Ar atmosphere in Figure 4a & b. The analysis revealed intriguing trends: the τ_2 peak decreased, indicating the decomposition of the interfacial passivation layer. Meanwhile, the τ_3 peak exhibited a pattern of initial increase followed by a decrease. This can be attributed to two opposing effects occurring simultaneously during the
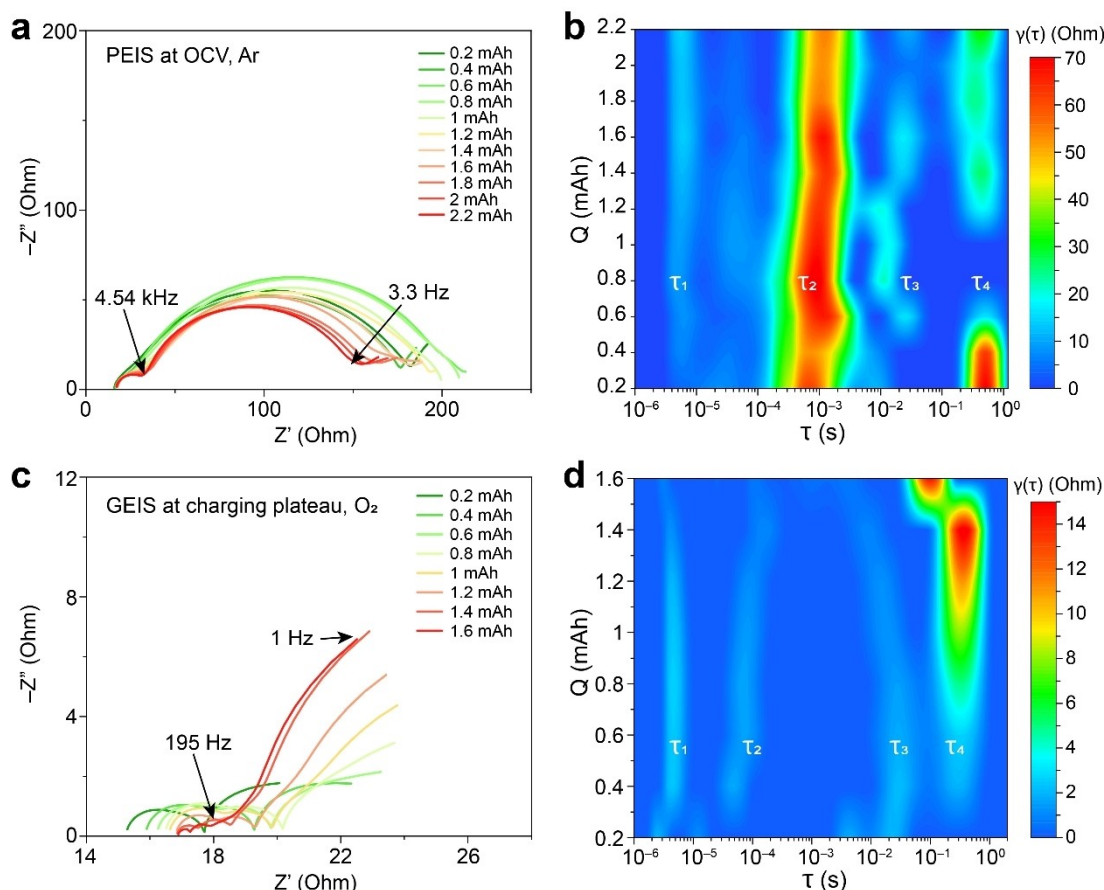
Batteries & Supercaps

Research Article
doi.org/10.1002/batt.202400257

Chemistry Europe
European Chemical
Societies Publishing

Figure 4. (a) Nyquist plots during charging at OCV under Ar. (b) Corresponding DRT analysis during charging at OCV under Ar. (c) Nyquist plots during charging at OCV under O_2. (d) Corresponding DRT analysis during charging at OCV under O_2.

decomposition process. Firstly, as $NaO_{x(ads)}$ decomposes, it loses contact with the solid electrode, causing an increase in the τ_3 peak. Secondly, the decomposition of $NaO_{x(ads)}$ releases more active sites on the surface, which tends to increase τ_3 peak. These conflicting effects result in the observed trend of τ_3 initially rising and then falling.

Conversely, τ_4 displayed a trend of initially decreasing, followed by an increase and subsequent decrease, which contrasts with the trend observed in τ_3 during charging. During charging, the solid-solid contact between cubic NaO_2 and the electrode surface initially reduces, leading to a decrease in the active surface area and consequently, a decrease in τ_4 (Figure 4b). In the mid-stage of charging, $NaO_{2(sol)}$ is dissolved at the outer surface, after which it diffuses to the electrode surface for oxidation and decomposition. With more reaction sites available on the surface, τ_4 increases. Additionally, during intermittent charging, a spike in the charging curve is observed after each rest period. This spike may be attributed to the re-establishment of connection between cubic NaO_2 and the active sites on the electrode surface during the rest. Initially, the solid contact interface decomposes, followed by the formation of new solid contact after rest, which passivates the active sites. However, these active sites for $NaO_{2(sol)}$ decomposition (Figure 4b) are restored once additional overpotential is applied.

Similarly, we utilized dynamic galvanostatic electrochemical impedance spectroscopy (GEIS) under O_2 to assess the deviation from the equilibrium state, which better reflects real charging conditions (Figure 4c & d). During the charging process, PEIS measured in argon gas is measured in OCV state, while GEIS measured in oxygen atmosphere is measured in charging platform. Due to the difference in potential, the low frequency impedance of the two is different. The overall trend closely resembles that of Ar-PEIS, but due to its higher operating voltage compared to open circuit voltage (OCV), which is akin to applying a charging overpotential, the charging transfer resistance (R_{ct}) of the charging reaction is lower overall than that of PEIS under Ar. Moreover, τ_3 exhibits a similar pattern of initially rising and then falling, mirroring the trend observed in Ar-PEIS.

However, τ_4 shows a different behavior, continuously increasing. This could be attributed to the higher potential providing a substantial overpotential for the initial solid-solid contact, thereby enabling the surface to possess more active sites earlier. This early increase in active sites is advantageous for the oxidation of $NaO_{2(sol)}$ in the middle and late stages, where $NaO_{2(sol)}$ oxidation becomes the predominant reaction during charging. As $NaO_{2(sol)}$ diminishes in size, the dissolution rate at the outer surface decreases, making it challenging to

provide enough $NaO_{2(sol)}$ for oxidation (Figure S5). Consequently, towards the end of charging, the decomposition of NaO_2 tends to be complete at the surface as the charging potential increases, resulting in a reduction of τ_4 at the end of the charging process.

It appears that the primary source of overpotential in Na-O_2 batteries does not directly come from the catalyst but rather from other factors. Specifically, the discharging overpotential arises mainly from the low concentration of oxygen and issues related to mass transport, whereas the charging overpotential predominantly originates from solid-solid contact.

To mitigate the discharging overpotential, efforts could focus on enhancing oxygen mass transport. This can be achieved by utilizing fluorinated solvents with high oxygen solubility and constructing hierarchically ordered pores to facilitate oxygen mass transport.

On the other hand, reducing charging overpotential requires attention to preventing the passivation of active sites at the electrode surface. This can be accomplished by designing additives to inhibit or slow down the formation of passivation products at the surface, thus ensuring continuous exposure of the active sites. Alternatively, enhancing the adsorption between the electrode and the product could also be beneficial. However, this approach may pose challenges as direct application of stack pressure to the porous electrode might not effectively transmit pressure to the space between the electrode and the product.

Conclusions

In our study, we investigated the origin of overpotential in Na–O_2 batteries during both discharging and charging processes using electrochemical impedance spectroscopy (EIS). Unlike lithium-ion batteries, the active area at the surface of Na-O_2 batteries undergoes continuous change, leading to a more complex distribution of relaxation time (DRT) peak.

Furthermore, we discovered that passivation layers, such as the solid electrolyte interface (CEI), have a relatively minor direct effect on ion transport on the electrode surface in Na-O_2 batteries. Instead, the main contributors to overpotential differ between discharging and charging processes. During discharging, overpotential primarily stems from oxygen mass transport, while during charging, it predominantly arises from poor solid-solid contact at the electrode surface.

Specifically, inadequate solid-solid contact during charging impedes the direct decomposition of solid product through charging, limiting the achievable current. Additionally, the formation of solid product passivates active reaction sites on the electrode surface, leading to a shortage of sites for decomposing the dissolved NaO_2 product, thus resulting in overpotential.

Our findings offer valuable insights for enhancing the performance of Na-O_2 batteries and can guide future efforts aiming at improving their efficiency and stability.

Experimental section

Configuration of Na–O_2 Battery

The experiment utilized an ether-based electrolyte. Benzophenone and sodium metal were added to diethylene glycol dimethyl ether (DEGDME, Aladdin, $>99\%$) in the glovebox overnight. Then the solvent was dried with sieves (4 Å) for several days. Sodium trifluoromethyl sulfonate (NaOTf, Sigma, $>98\%$) was dried under vacuum at 120 °C for 12 hours. The cathode consists of mixing conductive carbon black (Super P) and binder polytetrafluoroethylene (PTFE, 10 % aqueous suspension) in a ratio of 8:1 (wt.) to form a slurry. The slurry is then coated onto a stainless-steel screen (10 mm in diameter) and vacuum dried at 120 °C for 12 hours. The mass loading is 2 mg cm^{-2}. Metal sodium (Sigma) is used as the counter electrode, and silver chloride is employed as the reference electrode. 0.5 M NaOTf DEGDME served as the electrolyte. The electrolyte required to assemble the battery is approximately 500 μL. Besides, glass fiber filter membrane (Whatman) is the separator. The sodium carbonate (Na_2CO_3) and sodium peroxide (Na_2O_2) utilized in the experiment are manufactured by Sigma. A homebuilt Swagelok-type three-electrode battery was constructed with an oxygen reservoir column.

Electrochemical Measurements

The battery is assembled in an Ar-filled glovebox where oxygen and moisture concentration are below 0.1 ppm. The charging and discharging processes are performed in the same environment. Potentiostatic electrochemical impedance spectroscopy (PEIS) and dynamic galvanostatic electrochemical impedance spectroscopy (GEIS) tests were conducted by a VMP3 electrochemical workstation (Bio-Logic Ltd.) with a frequency range of 0.1 MHz–0.1 Hz and an amplitude of 10 mV (PEIS) and 100 μA (GEIS). Moreover, 0.2 mA was set at GEIS test to keep the battery at charge state. Additionally, 12 sample points were recorded in a frequency range of one order of magnitude at each interval. The current for both charging and discharging is 0.2 mA with discharge capacity smaller than 2 mAh, thereby obtaining a sodium superoxide (NaO_2) product. Specifically, EIS measurement was performed after standing for 1 h every time discharge capacity was up to 0.5 mAh. The parameters are the same for the charge periods except the capacity was cut off to 0.2 mAh. And the EIS test during charge was terminated once charge potential reached 2.8 V.

When seeking the DRT peak position linked to the charge transfer resistance, one can search for the DRT peak position by applying an overpotential of 50 mV in the positive or negative direction. In the calculation of DRT, we use the open Matlab code shared by Professor Francesco Ciucci, which is based on Tikhonov regularization. For DRT fitting parameter settings, we set the regularization parameter to 0.001 and regularize derivative to second order.

As to DEMS experiments, the positive electrode sheet after discharge were taken out and placed into a 10 μL empty vial. Then 0.3 ml of 1 M phosphoric acid(H_3PO_4) was added to determine the content of inorganic sodium carbonate (Na_2CO_3). Afterwards 0.5 M $FeSO_4$ and 20 μL of 30% H_2O_2 (Aladdin, AR, 30 wt.% in H_2O) were injected to measure the content of organic carbonate. When it comes to DEMS during charge to detect the specific gas evolution, the carrier gas Ar was set to 0.5 ml/min and rest for 30 min between gas detections.

Batteries & Supercaps

Research Article
doi.org/10.1002/batt.202400257

Chemistry Europe
European Chemical
Societies Publishing

Structure Characterization

Before Raman and SEM characterization, electrode samples were treated with acetonitrile. The surface topography was characterized by scanning electron microscope (SEM, Hitachi S-4800). The voltage was set to 5 kV, and current is 10 mA. The laser used is 532 nm in Raman spectroscopy (LabSpec-6-HORIBA).

Conflict of Interests

The authors declare no conflict of interest.

Data Availability Statement

The data that support the findings of this study are available from the corresponding author upon reasonable request.

[1] a) J. B. Goodenough, K.-S. Park, *J. Am. Chem. Soc.* **2013**, *135*, 1167–1176; b) M. He, K. C. Lau, X. Ren, N. Xiao, W. D. McCulloch, L. A. Curtiss, Y. Wu, *Angew. Chem. Int. Ed.* **2016**, *55*, 15310–15314; c) X.-H. L. Kai-Xue Wang, Jie-Sheng Chen, *Adv. Mater.* **2015**, *27*, 527–545; d) F. Li, S. Wu, D. Li, T. Zhang, P. He, A. Yamada, H. Zhou, *Nat. Commun.* **2015**, *6*, 7843; e) H. Liu, Z. Zhu, Q. Yan, S. Yu, X. He, Y. Chen, R. Zhang, L. Ma, T. Liu, M. Li, R. Lin, Y. Chen, Y. Li, X. Xing, Y. Choi, L. Gao, H. S.-y. Cho, K. An, J. Feng, R. Kostecki, K. Amine, T. Wu, J. Lu, H. L. Xin, S. P. Ong, P. Liu, *Nature* **2020**, *585*, 63–67; f) L. Qin, N. Xiao, S. Zhang, X. Chen, Y. Wu, *Angew. Chem. Int. Ed.* **2020**, *59*, 10498–10501; g) K. Song, D. A. Agyeman, M. Park, J. Yang, Y. M. Kang, *Adv. Mater.* **2017**, *29*, 1606572; h) J. Xie, Y.-C. Lu, *Nat. Commun.* **2020**, *11*, 2499; i) J. Chen, G. Zhang, J. Xiao, J. Li, Y. Xiao, D. Zhang, H. Gao, X. Guo, G. Wang, H. Liu, *Adv. Funct* **2023**, *34*; j) H. Gao, J.

Li, F. Zhang, C. Li, J. Xiao, X. Nie, G. Zhang, Y. Xiao, D. Zhang, X. Guo, Y. Wang, Y. M. Kang, G. Wang, H. Liu, *Adv. Energy Mater.* **2024**; k) Y. Xiao, J. Xiao, H. Zhao, J. Li, G. Zhang, D. Zhang, X. Guo, H. Gao, Y. Wang, J. Chen, G. Wang, H. Liu, *Small* **2024**.

[2] a) C. L. Bender, P. Hartmann, M. Vračar, P. Adelhelm, J. Janek, *Adv. Energy Mater.* **2014**, *4*, 1301863; b) P. Hartmann, C. L. Bender, M. Vračar, A. K. Dürr, A. Garsuch, J. Janek, P. Adelhelm, *Nat. Mater.* **2012**, *12*, 228–232; c) P. Hartmann, M. Heinemann, C. L. Bender, K. Graf, R.-P. Baumann, P. Adelhelm, C. Heiliger, J. Janek, *J. Phys. Chem. C* **2015**, *119*, 22778–22786.

[3] a) D. Langsdorf, T. Dahms, V. Mohni, J. J. A. Kreissl, D. Schröder, *Energies* **2020**, *13*, 5650; b) C. Xia, R. Fernandes, F. H. Cho, N. Sudhakar, B. Buonacorsi, S. Walker, M. Xu, J. Baugh, L. F. Nazar, *J. Am. Chem. Soc.* **2016**, *138*, 11219–11226; c) H. Yadegari, Q. Sun, X. Sun, *Adv. Mater.* **2016**, *28*, 7065–7093.

[4] a) O. Arcelus, C. Li, T. Rojo, J. Carrasco, *J. Phys. Chem. Lett.* **2015**, *6*, 2027–2031; b) X. Bi, R. Wang, K. Amine, J. Lu, *Small Methods* **2018**, *3*, 1800247; c) O. Sapunkov, V. Pande, A. Khetan, V. Viswanathan, *J. Phys. Chem. C* **2018**, *122*, 18829–18835.

[5] a) R. Black, A. Shyamsunder, P. Adeli, D. Kundu, G. K. Murphy, L. F. Nazar, *ChemSusChem* **2016**, *9*, 1795–1803; b) V. S. Dilimon, C. Hwang, Y.-G. Cho, J. Yang, H.-D. Lim, K. Kang, S. J. Kang, H.-K. Song, *Sci. Rep.* **2017**, *7*, 17635; c) S. Y. Sayed, K. P. C. Yao, D. G. Kwabi, T. P. Batcho, C. V. Amanchukwu, S. Feng, C. V. Thompson, Y. Shao-Horn, *Chem. Commun.* **2016**, *52*, 9691–9694.

[6] Y. S. Mekonnen, R. Christensen, J. M. Garcia-Lastra, T. Vegge, *J. Phys. Chem. Lett.* **2018**, *9*, 4413–4419.

[7] T. P. Heins, N. Schlüter, S. T. Ernst, U. Schröder, *Energy Technol.* **2019**, *8*, 1900279.

[8] a) L. Guo, P. C. Searson, *Electrochim. Acta* **2010**, *55*, 4086–4091; b) A. Mohammadi, L. Monconduit, L. Stievano, R. Younesi, *J. Electrochem. Soc.* **2022**, *169*, 070509; c) N. Zhang, S.-H. Yu, H. D. Abruña, *Chem. Commun.* **2019**, *55*, 10124–10127; d) K. Zhao, G. Fan, J. Liu, F. Liu, J. Li, X. Zhou, Y. Ni, M. Yu, Y.-M. Zhang, H. Su, Q. Liu, F. Cheng, *J. Am. Chem. Soc.* **2022**, *144*, 11129–11137.

[9] S. Meini, M. Piana, H. Beyer, J. Schwämmlein, H. A. Gasteiger, *J. Electrochem. Soc.* **2012**, *159*, A2135–A2142.

[10] X. Zhou, J. Huang, Z. Pan, M. Ouyang, *J. Power Sources* **2019**, *426*, 216–222.

[11] J. Illig, M. Ender, T. Chrobak, J. P. Schmidt, E. Klotz, E. Ivers-Tiffée, *J. Electrochem. Soc.* **2012**, *159*, A952–A960.

[12] J. Chen, E. Quattrocchi, F. Ciucci, Y. Chen, *Chem* **2023**, *9*, 2267–2281.

[13] a) I. Landa-Medrano, J. T. Frith, I. Ruiz de Larramendi, I. Lozano, N. Ortiz-Vitoriano, N. Garcia-Araez, T. Rojo, *J. Power Sources* **2017**, *345*, 237–246; b) M. M. Ottakam Thotiyl, S. A. Freunberger, Z. Peng, P. G. Bruce, *J. Am. Chem. Soc.* **2012**, *135*, 494–500; c) B. Schafzahl, E. Mourad, L. Schafzahl, Y. K. Petit, A. R. Raju, M. O. Thotiyl, M. Wilkening, C. Slugovc, S. A. Freunberger, *ACS Energy Lett.* **2017**, *3*, 170–176.